Catalysis Science & **Technology**



View Article Online PAPER



Cite this: Catal. Sci. Technol., 2018, 8, 5943

Received 4th July 2018, Accepted 9th October 2018

DOI: 10.1039/c8cy01392f

rsc.li/catalysis

Sintered precipitated iron catalysts with enhanced fragmentation-resistance ability for Fischer-Tropsch synthesis to lower olefins†

Yanping Chen, Youming Ni, D Yong Liu, Hongchao Liu, Xiangang Ma, Shiping Liu, Wenliang Zhu* and Zhongmin Liu **D**

Commercial precipitated iron catalysts suffer from severe fragmentation when applied in the Fischer-Tropsch to lower olefins reaction (FTO). Herein, sintered precipitated iron catalysts for FTO are prepared by varying the calcination temperature from 800 to 1400 °C to enhance their fragmentation-resistance ability. Compared with traditional precipitated iron catalysts, sintered precipitated iron catalysts require higher reduction temperatures to maintain high and stable activity and shift the production of hydrocarbons towards lower olefins. Spent sintered precipitated iron catalysts show bulk morphologies with less fragmentation than the fragmented and aggregated morphologies of spent traditional precipitated iron catalysts. The amount of coke inside the spent catalysts decreases from 41.8 to 12.5% as the calcination temperature increases from 500 to 1200 °C, and simultaneously, the chain length of soluble coke decreases from C₃₂ to C₂₁. The lower amount of coke and shorter chain length of soluble coke of the sintered precipitated iron catalysts come from the stronger mechanical strength-induced less space for coke accumulation during FTO, which further enhance the fragmentation-resistance ability of the catalysts.

1. Introduction

Lower olefins $(C_2^--C_4^-)$ are extensively used as essential building blocks. The direct conversion of syngas into lower olefins is always an attractive option and syngas can be obtained from coal, natural gas, or biomass which may relieve dependence on oil. The big challenge of the Fischer-Tropsch to lower olefins reaction (FTO) is the Anderson-Schulz-Flory (ASF) distribution of products which favours a broad distribution of hydrocarbons. 1-3 Recently, considerable progress has been made. The selectivity to lower olefins could reach 61% via the Fischer-Tropsch synthesis over carbon nanofiber-supported iron nanoparticles.4 Another notable significant achievement was the utilisation of a bifunctional catalyst ZnCrOx/MSAPO which realized a selectivity to lower olefins as high as 80%.5 The following investigation of bifunctional catalysts Zr-Zn/ SAPO-34 and Zn-ZrO₂/SSZ-13 demonstrated selectivities to lower olefins of 74% and 77%, respectively. 6,7 Another recent research study focused on cobalt carbide nanoprisms and a selectivity to lower olefins of 60% was achieved.8 All of these stud-

National Engineering Laboratory for Methanol to Olefins, Dalian National Laboratory for Clean Energy, Dalian Institute of Chemical Physics, Chinese Academy of Sciences, Dalian 116023, P.R. China. E-mail: wlzhu@dicp.ac.cn, liuzm@dicp.ac.cn; Fax: +86 411 84379289; Tel: +86 411 84379998 † Electronic supplementary information (ESI) available: Programmed temperature of calcination, pore diameter distribution, catalytic performance, and chain growth probability. See DOI: 10.1039/c8cy01392f

ies are significantly meaningful for the direct conversion of syngas into lower olefins and investigations into their potential commercial applications are in progress.

The improvement of current commercial catalysts is also an effective approach for the industrial development of FTO. There are two classes of known commercial iron catalysts for the Fischer-Tropsch synthesis which have been used in industry for many years: fused iron catalysts and precipitated iron catalysts. 9,10 Fused iron catalysts are used in hightemperature Fischer-Tropsch (HTFT) reactions with reaction temperatures of 330-350 °C in fluidized bed reactors for production of gasoline and lower olefins, and precipitated iron catalysts are applied in low-temperature Fischer-Tropsch (LTFT) reactions with reaction temperatures of 200–240 °C in slurry reactors for production of high molecular mass waxes. 10-13 Fused iron catalysts can be operated in a hightemperature fluidized state thanks to their strong mechanical strength, so they seem to be an interesting option for FTO which favours relatively high temperatures (≥280 °C). Potassium and manganese are essential promoters for shifting the production of hydrocarbons towards lower olefins. 14-17 The size of the manganese ion is similar to that of the iron ion, so manganese ions can replace iron ions in the iron oxide lattice. However, potassium ions are too large to fit into the iron oxide lattice structure and tend to aggregate into small inclusions inside the iron phase during the solidification process of fused iron catalysts. 9,18-21 Hence, the distribution of

potassium in fused iron catalysts is very heterogeneous which makes them not a good choice for FTO.

Precipitated iron catalysts are prepared from metal ion solution which can ensure a uniform distribution of potassium and their high surface areas can compensate for the low activity of LTHT reactions. There is no fragmentation of catalysts as a result of little or no carbon deposition at low reaction temperatures. However, the great challenge for the application of precipitated iron catalysts in FTO is the fragmentation of catalysts induced by coke of carbon deposition and hydrothermal sintering at high reaction temperatures.²² The Boudouard reaction (2CO \rightarrow C + CO₂ or CO + H₂ \rightarrow C + H₂O) is considered to be the key reaction resulting in carbon deposition.²³⁻²⁶ Its activation energy is 113 kJ mol⁻¹, higher than that of 89.1 kJ mol⁻¹ of the Fischer-Tropsch reaction, thus it is more sensitive to the increase of reaction temperature. 9,23,27 The rate of carbon deposition increased tenfold when the reaction temperature rose from 285 to 338 °C, and the corresponding carbon species evolved from amorphous carbon to graphitic carbon. 9,23

A previous study by Shroff²⁸ showed that a spent precipitated Fe/Cu/K catalyst was broken down into small crystallites of carbide phases because of the deposition of carbon and the small carbide crystallites were covered with a layer of carbon with a thickness of a few nanometers. A recent research study of De Jong's group4 further showed that fragmentation of a precipitated Fe/Ti/Zn/K catalyst was observed in FTO due to the fibril or filament-shaped carbon deposition. A subsequent investigation by Liu²⁹ using environmental transmission electron microscopy has visualized the continuous graphitic carbon growth on the surface of iron carbide phases and the subsequent mechanical degradation as a result of breakage of nanoparticles into smaller pieces. Fragmentation of particles of precipitated iron catalysts may plug fixed-bed reactors or foul the separation apparatus in fluidized-bed reactors. Therefore, iron catalysts for FTO with enhanced fragmentation-resistance ability and simultaneous well distributed potassium are under urgent development.

Thus, in this paper, sintered precipitated iron catalysts were investigated to fulfil the requirements of catalysts with good fragmentation-resistance ability and well distributed potassium. Various sintered precipitated iron catalysts were obtained with calcination temperatures ranging from 800 to 1400 °C. The fragmentation-resistance ability was investigated by the characterization of the morphologies and coke accumulation of spent catalysts.

2. Experimental

2.1 Synthesis of sintered precipitated iron catalysts

The total preparation can be divided into two steps. The first step is the preparation of precipitated precursors. 40.0 g of ferric nitrate Fe(NO₃)_{3b}·9H₂O and 1.0 g of Mn(NO₃)₂·4H₂O were dissolved in 100.0 g of distilled water. The obtained nitrate solution and ammonia solution (25 wt%) were dropped alternately into a beaker with continuous stirring at pH 9.0,

which was placed in a water bath at 80 °C. The precipitates were filtered and washed with distilled water till pH 7.0. 13.9 g of 1 wt% K2CO3 solution was added to the washed precipitates, followed by stirring for 10 min and evaporation. The residue was dried at 100 °C and then the precipitated precursors were obtained. The second step is the sintering process. The precursors were calcined at different temperatures, following the programmed temperatures listed in Table S1.† Taking 1000-calcin for example, the initial temperature was 20 °C, and then the temperature was increased to 100 °C after 60 min, then to 250 °C after 30 min, and to 400 °C after 60 min, and held at this temperature for 120 min. The temperature was continuously increased to 1000 °C after 240 min, and held at this temperature for 300 min. Finally, the catalyst was cooled down to room temperature, and the sintered precipitated iron catalyst 1000-calcin was obtained. The prepared catalyst was milled and sieved into 40-60 mesh. Meanwhile, the first step for 1400-calcin-mix was physical mixing of Fe(NO₃)₃·9H₂O, Mn(NO₃)₂·4H₂O and K₂CO₃ and the second step followed the sintering process. The sintering process was operated in a box-type resistance furnace under a power of 8 kW with a silicon controlled temperature controller. A traditional precipitated iron catalyst denoted as 500calcin was used as a reference catalyst. The sintered precipitated iron catalysts were denoted as 800-calcin, 1000-calcin, 1200-calcin, and 1400-calcin. 1400-calcin-mix was used as a reference fused iron catalyst. The composition of all the catalysts was adjusted to 100Fe/4Mn/2K.

2.2 Characterization

X-ray diffraction (XRD) patterns were recorded on a PANalytical X'Pert PRO X-ray diffractometer using Cu Kα radiation with a working voltage of 40 kV and a current of 40 mA. The reducibility of the samples was studied by temperatureprogrammed reduction in hydrogen (H2-TPR) and the whole process was detected by in situ XRD on a Rigaku X-ray diffractometer equipped with an Anton-Paar XRK-900 reaction chamber. 10% H₂/N₂ was used as the reducing gas with a flow of 30 ml min⁻¹ at atmospheric pressure and the temperature range was 250-800 °C. Diffraction patterns were recorded within the 2θ range of $20-70^{\circ}$ with a scanning rate of 10° min⁻¹. The heating rate of 500-calcin and 1400-calcinmix was 2 and 5 °C min⁻¹, respectively. The heating rate of 800-calcin, 1000-calcin, 1200-calcin, and 1400-calcin was 3 °C min⁻¹. The morphology of the samples was examined using scanning electron microscopy (SEM) on a JEOL JSM-5600 LV system. Textural properties were measured by N2 adsorption porosimetry on a Micromeritics ASAP2020 system. The surface area was calculated using the BET equation. The mesopore size distributions were determined according to the Barrett-Joyner-Halenda (BJH) method. Thermogravimetric (TG) analysis was performed on a TA SDTQ600 analyzer with a temperature programmed rate of 10 °C min⁻¹ under an air flow of 100 ml min⁻¹ and mass spectrometry (MS) was carried out on a Thermo Star. The spent samples were dissolved with

a CH₂Cl₂ solution (20.0 wt%) to identify coke species. The solution obtained was analyzed by gas chromatography-mass spectrometry (GC-MS) on an Agilent GC6890-MS5973.

2.3 Catalytic test

The catalytic reaction was performed using a fixed-bed stainless steel reactor with 0.8 g of catalyst diluted with 0.8 g of silica sand (40-60 mesh) at a gas hourly space velocity (GHSV) of 4000 h^{-1} . The reaction conditions: $H_2/CO = 1$ (molar ratio), 1.5 MPa, time on stream (TOS) = 8 h, and reaction temperature = 310 °C. 4% Ar in CO was used to calculate the CO conversion. Prior to the reaction, the catalysts were firstly reduced at certain temperatures by pure hydrogen for 12 h with a GHSV of 4000 h⁻¹. The reduction temperature varied between 300 and 550 °C according to different samples. An online Agilent 7890A gas chromatograph (GC) was used to analyze the products. Hydrocarbon products were analyzed with an HP-PLOT/Q capillary column (30 m × 0.32 mm) and a flame ionization detector (FID). H2, CO, Ar, CH4 and CO2 were measured with a TDX-01 packed column (2 m × 2 mm) and a thermal conductivity detector (TCD). Lines and valves before GC were heated to maintain the temperature at 160 °C to prevent possible condensation of products. The carbon balance was better than 95%.

3. Results and discussion

3.1 Catalyst characterization

The sintering of Fe₂O₃ can be achieved above its Tammann temperature of 626-783 °C, thus the sintered precipitated iron catalysts have been obtained with calcination temperatures ranging from 800 to 1400 °C. The morphology of traditional and sintered precipitated iron catalysts is shown in Fig. 1. The traditional precipitated iron catalyst 500-calcin was composed of nanoparticles which were uniform in size and shape, with a mean diameter of 20-40 nm (Fig. 1(A)), well in line with references.³⁰⁻³² The particle diameter of 800calcin increased to 50-200 nm because of sintering at the calcination temperature of 800 °C. 1000-calcin, 1200-calcin, 1400-calcin and 1400-calcin-mix demonstrated integral morphologies indicating more severe sintering as the calcination temperature increased.

The N₂ adsorption-desorption isotherms of 500-calcin and 800-calcin are shown in Fig. S1.† The shape of the hysteresis loops and the trend of the isotherm of 500-calcin were identified as type IV, which was characteristic of mesoporous materials. The mean diameter of 500-calcin was 9.91 nm and the surface area was 59.84 m² g⁻¹ (Fig. S2 and Table S2†). The high surface area resulted from the intergranular space among uniform nanoparticles. The hysteresis loops of 800calcin shifted to a higher relative pressure and the surface area decreased to 6.77 m² g⁻¹, corresponding to larger particles in Fig. 1(B). So it can be concluded that there are no mesopores inside the sintered precipitated iron catalysts.

The XRD patterns of the traditional and sintered precipitated iron catalysts without reduction are shown in Fig. 2.

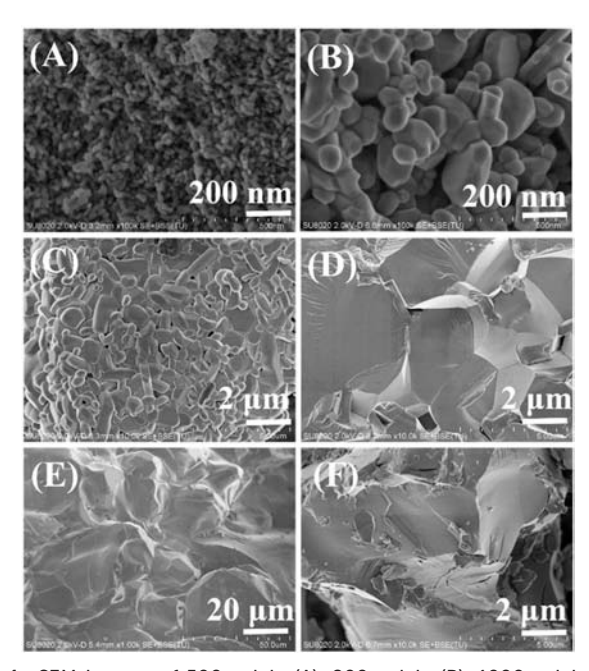


Fig. 1 SEM images of 500-calcin (A), 800-calcin (B), 1000-calcin (C), 1200-calcin (D), 1400-calcin (E), and 1400-calcin-mix (F) catalysts.

The α -Fe₂O₃ crystal phase was detected in all the catalysts, yet the diffraction peaks of the sintered precipitated iron catalysts were slightly narrower than those of the traditional precipitated iron catalyst 500-calcin, indicating the formation of larger sizes of α-Fe₂O₃ crystals induced by sintering. The reducibility and iron phase transformation of the traditional and sintered precipitated iron catalysts are monitored in situ by XRD during H₂-TPR, as shown in Fig. 3. The temperature ranges of the existence and co-existence of various iron phases are listed in Table 1 according to in situ XRD. For 500-calcin, the iron phases varied with the increase of reduction temperature. The first transformation of iron phases was the reduction of Fe₂O₃ to Fe₃O₄. Fe₂O₃ started to be reduced into Fe₃O₄ at 306 °C, and the reduction continued until Fe₂O₃ was completely reduced into Fe₃O₄ at 386 °C, which indicated the co-existence of Fe₂O₃ and Fe₃O₄ between 306 and 386 °C. Only the Fe₃O₄ phase existed between 386 and 496 °C demonstrating the temperature range of its stable existence. The second transformation of iron phases was the reduction of Fe₃O₄ to FeO. The initial reduction of Fe₃O₄ to FeO occurred at 496 °C, and Fe₃O₄ continued to be converted to FeO with the reduction temperature increasing to 536 °C. The final iron phase evolution was the reduction of FeO to Fe. FeO was initially transformed into Fe at 536 °C and completely into Fe at 616 °C, and then Fe existed as a single phase above 616 °C. Temperatures of H₂-TPR of 500-calcin are consistent with those of precipitated iron catalysts in the literature; 30,33 furthermore, the in situ XRD provides additional iron phase evolution during H2-TPR.

The sintered precipitated iron catalysts followed the same trend of the iron phase evolution as the traditional precipitated iron catalyst 500-calcin. However, when the calcination

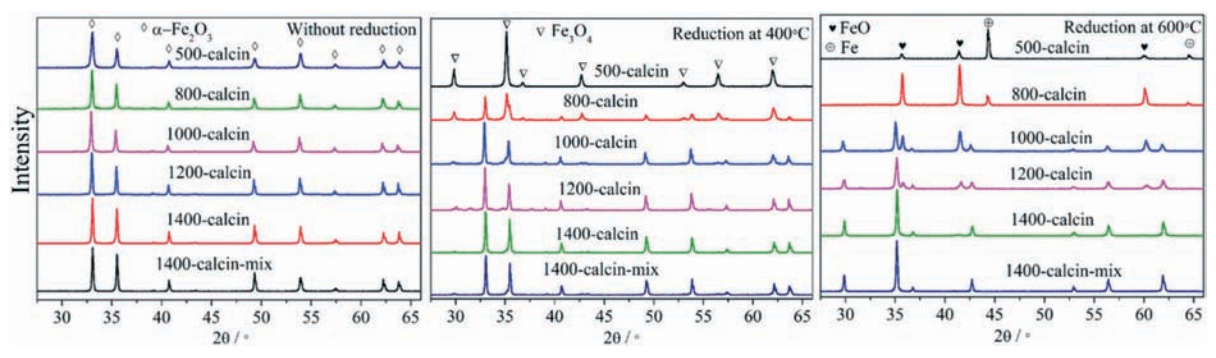


Fig. 2 XRD patterns of traditional and sintered precipitated iron catalysts without reduction and with reduction at 400 and 600 °C.

temperature rose from 500 to 1400 °C, the temperature ranges of transformation of Fe₂O₃ to Fe₃O₄, Fe₃O₄ to FeO, and FeO to Fe increased from 306-386 °C to 487-532 °C, 496-536 °C to 637-702 °C, and 536-616 °C to >775 °C, respectively. Simultaneously, the temperature ranges of the existence of the single iron phases Fe₃O₄ and FeO increased from 386-496 °C to 532-637 °C and 550-585 °C to 702->775 °C. The peak intensity of the XRD patterns and the states of the iron phases of all the catalysts after temperatureprogrammed reduction at 400 and 600 °C can be compared in Fig. 2. After reduction at 400 °C, 500-calcin exhibited a single Fe₃O₄ phase, and 800-calcin underwent transformation from Fe₂O₃ to Fe₃O₄, yet the other sintered precipitated iron catalysts still remained in the Fe₂O₃ phase. After reduction at 600 °C, the main iron phases of 500-calcin and 800-calcin were Fe and FeO, respectively, with small amounts of FeO in 500-calcin and Fe in 800-calcin. The main iron phase of 1000calcin and 1200-calcin was Fe₃O₄, with a small amount of FeO in 1000-calcin and an even smaller amount in 1200calcin. Fe₃O₄ existed as a single phase in 1400-calcin and 1400-calcin-mix. Obviously, the reducibility of the sintered precipitated iron catalysts becomes poorer and poorer as the calcination temperature increases.

The poor reducibility of the sintered precipitated iron catalysts was related to their physical properties. The diameter of particles of 800-calcin was 0.05-0.2 µm and that of 1000calcin, 1200-calcin, 1400-calcin, and 1400-calcin-mix was 250-425 µm (40-60 mesh) which was the desired mean size of particles for the catalytic test through crushing and milling, much larger than 20-40 nm of 500-calcin. On the other hand, the higher calcination temperature caused severe sintering of the Fe₂O₃ phase leading to denser and more solid structures of the catalysts.

Sintered precipitated iron catalysts with large-sized particles and dense structures are more inclined to follow the shrinking core model of reduction, that is, the reduction proceeds from the outside towards the core of the catalyst. 34-37 During reduction of the sintered precipitated iron catalysts, α-Fe₂O₃ undergoes transformation to Fe₃O₄ and FeO before being fully reduced to Fe with the reduction temperature increasing; simultaneously and competitively, the formed α-Fe can be oxidized into Fe₃O₄ again by H₂O which is produced during the reduction process.9 The amount of formed H2O from α-Fe₂O₃ to Fe₃O₄ during the reduction process is half of that from Fe₃O₄ to FeO and one sixth of that from FeO to Fe (ESI,† eqn (1)-(3)), which means that the higher the reduction degree of Fe₂O₃, the higher the H₂O/H₂ partial pressure ratio. Furthermore, from the point of view of the shrinking core model of reduction, the closer the position to the core of particles, the poorer the diffusion of H2 into the position and the worse the escape of H₂O out the position, leading to a higher H₂O/H₂ partial pressure ratio of the core of particles. Kock³⁸ showed that if $H_2O/H_2 = 1$, the reduction of α -Fe₂O₃ to metallic iron was impossible below 1000 °C. Higher reduction temperatures can accelerate diffusion of H2 and H2O and decrease the H₂O/H₂ partial pressure ratio in the core of particles, achieving complete reduction, which plays a considerably important role in the subsequent catalytic activity.

3.2 Catalytic activity

Fig. 4(A) shows the activity evolution of 500-calcin and 800calcin with different temperatures of reduction. Apparently, the reduction temperature played an important role in the activity and stability of the catalysts. In the case of the 800calcin catalyst, the lower CO conversion at the reduction temperature of 300 °C was induced by an inadequate reduction of the catalyst. Reduction temperatures of 320, 340, 360, and 400 °C could result in a high initial CO conversion of 97%, yet the CO conversion dropped to 72, 82, 88, and 92%, respectively, after reaction for 8 h. Evidently, higher and more stable activity can be achieved through increasing reduction temperature. The different activities of 800-calcin with various reduction temperatures could be related to the evolution of the iron phases during FTO. More recent studies by Chen's group³⁹ have investigated the effect of reduction temperature on the evolution of iron phases of a fused iron catalyst during Fischer-Tropsch synthesis. XRD and Mössbauer spectroscopy were used to quantitatively determine the phase composition of the spent catalyst with various reduction temperatures. They revealed that the higher the reduction temperature, the larger the amount of the formed active phase Fe₅C₂ at the initial stage of reaction, and the smaller the amount of regenerated Fe₃O₄ from the Fe₅C₂ phase as the

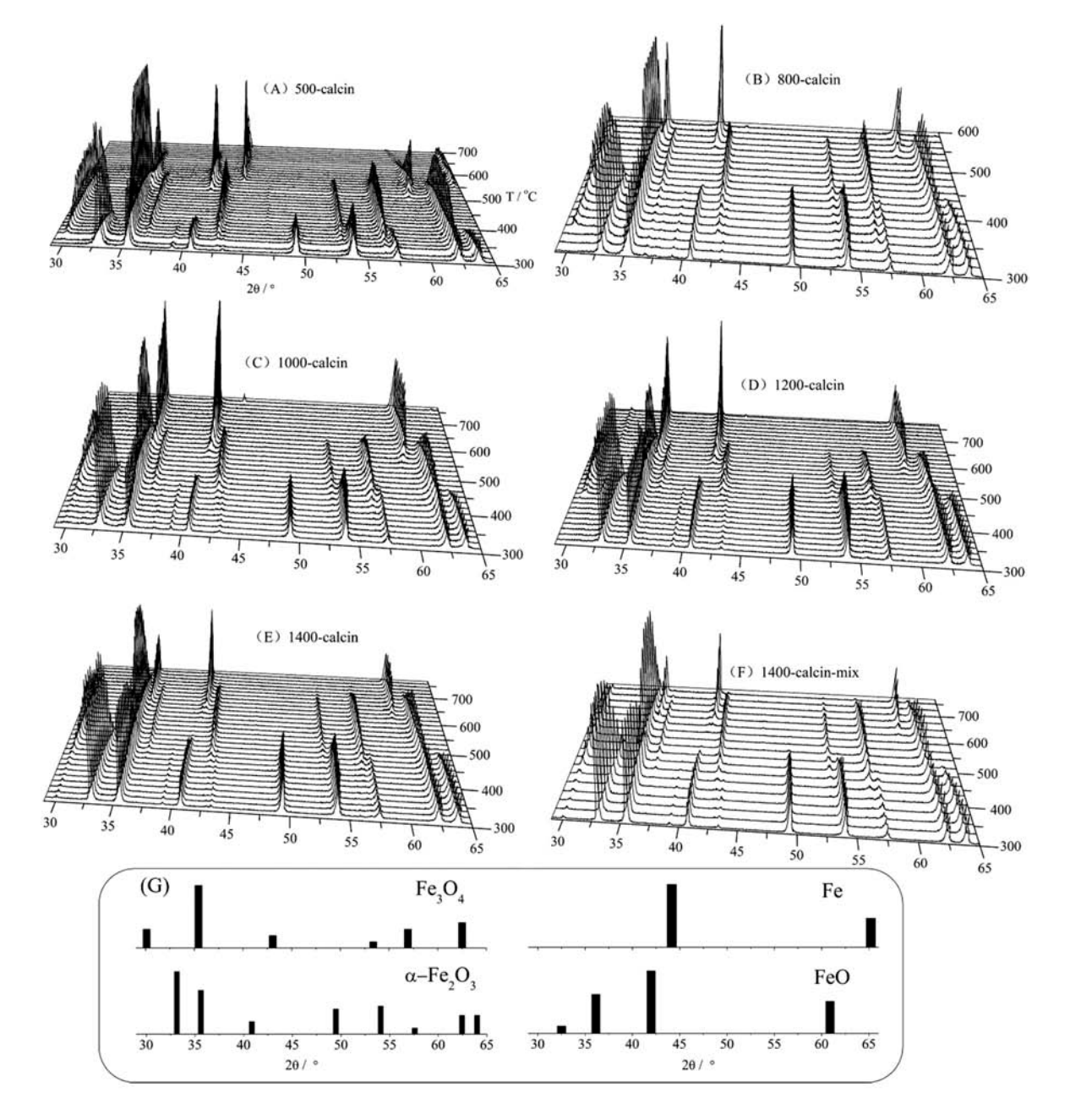


Fig. 3 Temperature-programmed reduction of 500-calcin (A), 800-calcin (B), 1000-calcin (C), 1200-calcin (D), 1400-calcin (E), and 1400-calcinmix (F) in 10% H₂/N₂ monitored in situ by XRD and main peaks of standard XRD of iron and iron oxides (G).

Table 1 Temperature ranges of the existence and co-existence of iron phases in TPR of traditional and sintered precipitated iron catalysts by $10\% H_2/$ N₂ monitored in situ by XRD

Catalysts	Fe_2O_3 , $Fe_3O_4/^{\circ}C$	$\mathrm{Fe_3O_4/^{\circ}C}$	Fe ₃ O ₄ , FeO/°C	FeO/°C	FeO, Fe/°C	Fe/°C
500-calcin	306-386	386-496	496-536	_	536-616	616-700
800-calcin	347-430	430-505	505-550	550-585	585->775	_
1000-calcin	432-515	515-547	547-622	622-752	752->775	_
1200-calcin	470-522	522-577	577-657	657->775	>775	_
1400-calcin	487-532	532-637	637-702	702->775	>775	_
1400-calcin-mix	435-540	540-645	645-745	745->775	>775	_

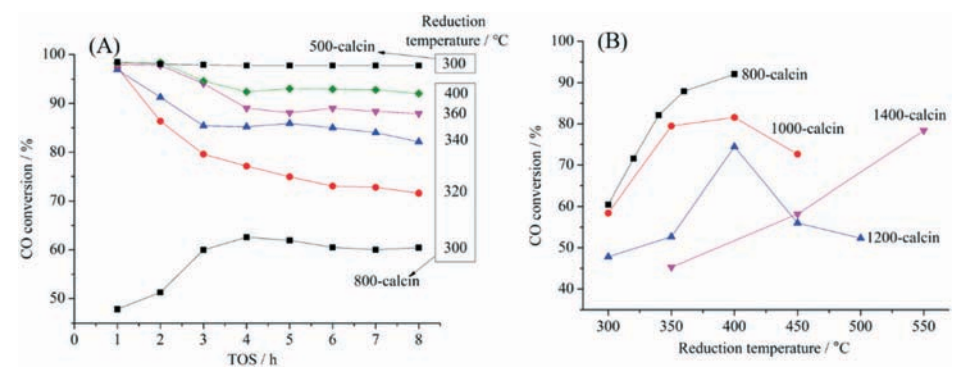


Fig. 4 Activity evolution of 500-calcin and 800-calcin during FTO (A) and effect of reduction temperature on the activity of sintered precipitated iron catalysts (B). Reaction conditions: $H_2/CO = 1$; 1.5 MPa; 310 °C; GHSV = 4000 h⁻¹; TOS = 8 h.

reaction proceeded. Analysis of individual fused iron particles showed that the core of the particles was more oxidized than the outer layers due to the difficult escape of the formed H₂O and CO₂ from the core as the Fischer–Tropsch reaction proceeded. Thus, the regenerated Fe₃O₄ can be related to the oxidized atmosphere of the core of fused iron particles during Fischer–Tropsch synthesis. Fused iron catalysts and sintered precipitated iron catalysts may undergo similar evolution of iron phases in FTO due to their similar large-sized particles and strong mechanical properties.

By comprehensive consideration of the reduction temperature and transformation of iron species during reduction by hydrogen (Fig. 3 and Table 1), the diverse activity of 800calcin at different reduction temperatures (Fig. 4(A)), and the evolution of iron phases of the sintered precipitated iron catalysts, the schematic evolution of different iron species of 800-calcin can be obtained (Fig. S4†). The evolution of iron species started from the outside towards the core of particles. Firstly, the outside layer of Fe₂O₃ particles was completely reduced into metallic iron and the core was reduced into Fe₃O₄ by hydrogen. The thickness of the formed metallic iron layer varied with different reduction temperatures. Secondly, when the formed metallic iron came into contact with syngas, it dissociated CO and dissolved carbon in its crystal interstices, forming Fe₅C₂ which was commonly believed to be the active phase of FTO, 41,42 yet the core of Fe₃O₄ remained unchanged which was considered as an inactive phase for FTO. Fe₃O₄ could be obtained at lower reduction temperatures and remain relatively stable during FTO. Thirdly, as the reaction proceeded, the inside layer of formed Fe₅C₂ was oxidized into Fe₃O₄ by H₂O and CO₂ formed during FTO, namely, regenerated Fe₃O₄, which was also inactive for FTO. When the reduction temperature increased from 320 to 400 °C, it seemed that the higher the reduction temperature, the thicker the outside layer of metallic iron after reduction by hydrogen, that is, the higher the amount of formed metallic iron, the higher the amount of formed Fe₅C₂ after a one-hour reaction, and the smaller the amount of regenerated Fe₃O₄ after eight hours of reaction. Thus, the trend of the CO conversion curve of 800-calcin can be fully explained by the schematic evolution of iron species. In the case of the reduction temperature of 300 $^{\circ}$ C, only a thin layer outside the catalyst was completely reduced into metallic Fe, which was the reason for the low CO conversion. The increase of CO conversion at the initial two hours might be due to the further reduction of the catalyst by syngas. It should be noted that the Fe₂O₃ phase of 800-calcin could be fully reduced into the metallic iron phase at the reduction temperature of 400 $^{\circ}$ C.

The activity evolution of 1000-calcin, 1200-calcin, and 1400-calcin (Fig. S3†) was similar to that of 800-calcin, thus the evolution of their iron phases was similar to that of 800calcin. Sintered precipitated iron catalysts 800-calcin, 1000calcin, and 1200-calcin can achieve maximum activity at the reduction temperature of 400 °C (Fig. 4(B)). When the reduction temperature was below 400 °C, the activity of the catalysts increased and the inactivity slowed down with the increase of the reduction temperature. When the reduction temperature was above 400 °C, the inactivity of the catalysts was accelerated by the increase of the reduction temperature due to the hydrothermal sintering-induced large crystals of iron phases during FTO (Fig. S4†). The hydrothermal sintering-induced large crystals of iron phases at the reduction temperature of 450 °C are well in line with results of Dry9 and Chen's groups.39 However, the sintered precipitated iron catalyst 1400-calcin required a reduction temperature of 550 °C for complete reduction. The calcination temperature of 1400 °C is close to the fusion point of Fe₂O₃ of 1565 °C which may lead to fusion of 1400-calcin and cause similar properties of fused iron catalysts. Chen's group³⁹ showed that the initial CO + H2 conversion of fused iron catalysts increased as the reduction temperature increased monotonously from 350 °C to 650 °C, which is exactly similar to the CO conversion of 1400-calcin in our study.

3.3 Catalytic selectivity

Fig. 5 shows the product distribution of the traditional and sintered precipitated iron catalysts. As reported by a considerable number of literature studies, for iron-based catalysts, the promoter potassium provides electrons to iron and hence accelerates the adsorption and dissociation of CO resulting in a lower methane selectivity and a higher olefin/paraffin (O/

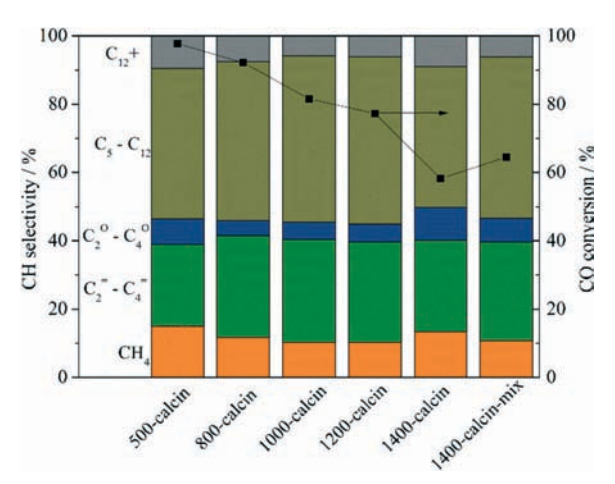


Fig. 5 Product distributions of traditional and sintered precipitated iron catalysts. Reduction conditions: H₂; 12 h; GHSV = 4000 h⁻¹; 500calcin: 300 °C; 800-calcin, 1000-calcin, and 1200-calcin: 400 °C; 1400-calcin and 1400-calcin-mix: 450 °C. Reaction conditions: H₂/CO = 1; 1.5 MPa; TOS = 8 h; 310 °C; GHSV = 4000 h^{-1}

P) ratio in FTO. Therefore, a suitable potassium level or a more uniform distribution of potassium is essential for production of lower olefins. 14,16,43

The sintered precipitated iron catalysts 800-calcin, 1000calcin, and 1200-calcin demonstrated lower methane selectivity, higher O/P ratios of C2, C3, and C2-C4, and simultaneously higher $C_2 = -C_4$ selectivity than the traditional precipitated catalyst 500-calcin, as shown in Fig. 5 and 6. The potassium content of the sintered and traditional precipitated iron catalysts was the same, hence the plausible explanation was 800-calcin, 1000-calcin, and 1200-calcin exhibited a more uniform distribution of potassium than 500-calcin. The better distribution of potassium of the sintered catalysts can be interpreted as follows: potassium exists as a separate phase of occlusions inside the iron-manganese phase due to its large size which is not suitable for the iron oxide lattice.⁹ The denser and stronger mechanical strength of the sintered

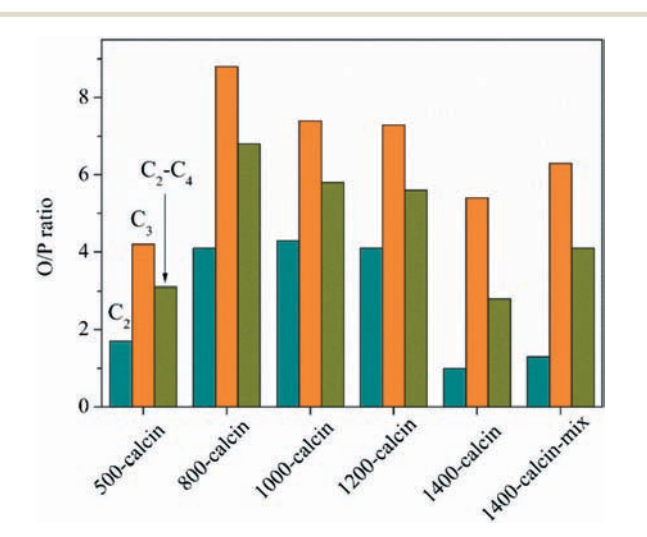


Fig. 6 O/P ratios of C_2 , C_3 , and C_2 – C_4 of traditional and sintered precipitated iron catalysts.

precipitated iron catalysts prohibits the separation of potassium occlusions from the iron-manganese phase and further suppresses their subsequent aggregation into large particles due to hydrothermal sintering during FTO, namely, suppressing the "fluxing" effect of potassium and resulting in well distributed potassium. Compared with 1000-calcin and 1200calcin, 800-calcin demonstrated slightly higher O/P ratios of C₃ and C₂-C₄, which would be related to its smaller-sized particles maximizing the effect of the potassium distribution and simultaneously balancing the surface areas of iron species.

However, the sintered catalyst 1400-calcin demonstrated higher methane selectivity, lower O/P ratios of C2, C3, and C_2 - C_4 and simultaneously lower C_2 - C_4 selectivity than 800calcin, 1000-calcin and 1200-calcin, which indicated a poorer distribution of potassium. The calcination temperature of 1400 °C is close to the fusion point of α -Fe₂O₃ of 1565 °C, thus 1400-calcin exhibited lower selectivity to lower olefins than the fused iron catalyst 1400-calcin-mix. During the fusion process of fused iron catalysts, all components experience a disordered liquation state and potassium tends to grow into large sizes of particles during the solidification process, which are easy to separate from the iron-manganese phase during the milling process. Previous literature studies reported that 9,20,21 the larger particles of milled potassiumpromoted fused catalysts contained potassium occlusions inside iron oxide phases, while the finer particles consisted of a mixture of separate potassium and iron oxide particles. In confirmation, they also showed that the performance of potassium-promoted fused iron catalysts in the Fischer-Tropsch reaction was fairly similar to that of physically mixed milled fused iron oxides and potassium silicates. 1400-calcinmix demonstrated a slightly lower methane selectivity and a higher selectivity to lower olefins than 1400-calcin which might be due to the nitrate ion playing a positive role in the potassium distribution during the fusion process, consistent with its slightly lower reduction temperature in Table 1 and higher CO conversion in Fig. 5. The α values of chain growth probability of all the catalysts are shown in Table S3.† The α values of the potassium-promoted catalysts were all around 0.7, similar to those of industrial fused iron catalysts in HTFT reactions (Table S4†). The CO₂ selectivity of the sintered precipitated iron catalysts was around 27%, slightly lower than that of 500-calcin, due to the well distributed potassium suppressing the water gas shift (WGS) reaction. Compared with the hydrocarbon distribution of bulk iron catalysts in literature reports (Table S4†) and our prepared traditional precipitated iron catalysts, the sintered precipitated iron catalysts shift the production of hydrocarbons towards lower olefins.

3.4 Characterization of spent catalysts and coke species

Fig. 7 shows the morphology of the spent traditional and sintered precipitated iron catalysts. The spent 500-calcin catalyst was mainly composed of aggregated (Fig. 7(A)) and fragmented (7(B)) particles with sizes ranging from 50 to 200

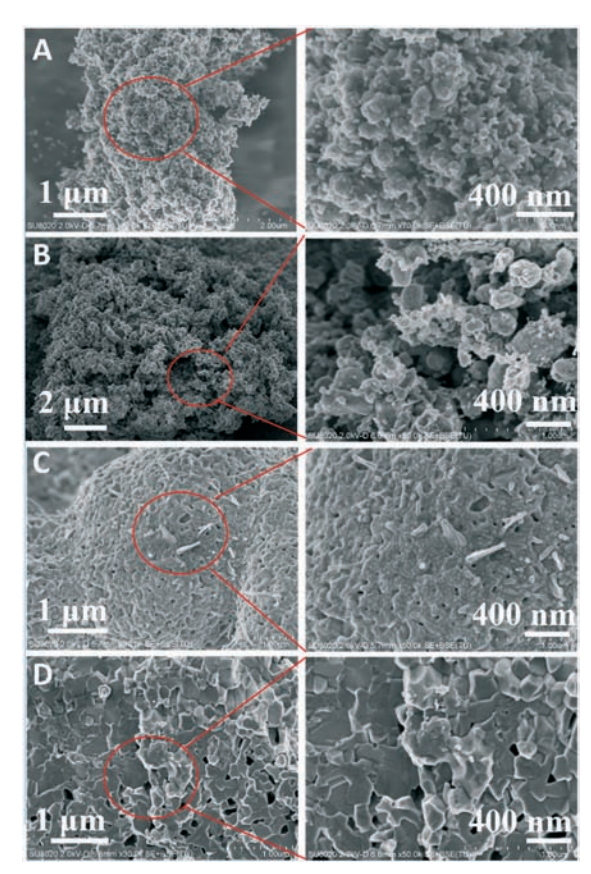


Fig. 7 Morphology of aggregated (A) and fragmented particles (B) of spent 500-calcin and particle surfaces of spent 1200-calcin (C) and 1400-calcin (D) catalysts

nm or even more. The aggregated particles were caused by hydrothermal sintering during FTO. The fragmented particles were loose and fragile, with a broad distribution of particle sizes and complicated shapes. The fragmentation of 500calcin could be ascribed to the initial deposition of graphitic coke and then the continuous build-up of long-chain wax of coke within the catalyst pores. Previous studies^{44,45} showed that the XRD patterns of spent traditional precipitated iron catalysts were broad and indistinct, confirming the presence of very small crystals of iron carbides. The spent 1200-calcin remained as a bulk with less fragmentation, as shown in Fig. 7(C). There were a lot of pores on the surface of 1200calcin which could be due to channel development as oxygen atoms were eliminated during the reduction process.^{9,39} The porous surface is in agreement with investigations by Chen's group, 9,39 who studied the morphology of a reduced fused iron catalyst and found some pores on the surface. From Fig. 7(D), it can be seen that the spent 1400-calcin provided some larger pores on the surface compared with the spent 1200-calcin due to its stronger mechanical strength. Generally speaking, the sintered precipitated iron catalysts demonstrate simple evolution of morphology with less fragmentation. The decreased surface area of the spent 500-calcin (Fig. S1 and Table S2†) was due to the aggregation of nanoparticles, consistent with the SEM results in Fig. 7(A). The textural properties of non-porous 800-calcin didn't change after FTO.

The TG weight loss and differential thermal analysis (DTA) of spent 500-calcin, 800-calcin and 1200-calcin catalysts are shown in Fig. 8(A)-(C). TG degradation and DTA of all the catalysts could be basically divided into three decomposition stages, and the corresponding combustion temperatures and weight losses of each decomposition stage are shown in Table S5.† The combustion temperatures shifted from 260-314 °C to 250-340 °C for the first decomposition stage, from 314-370 °C to 340-440 °C for the second stage, and from 370-409 °C to 440-473 °C for the third stage, as the calcination temperature rose from 500 to 1200 °C. There is no trend for weight losses of each decomposition stage of the three catalysts, yet, the total weight losses decreased from 41.8% of 500-calcin to 31.0% of 800-calcin, and then to 12.5% of 1200calcin. Similar to 500-calcin, Dry^{9,18} concluded that the spent precipitated iron catalysts from both the fixed and slurry bed reactors contain about 50-60 wt% coke inside the catalysts. The weight losses and combustion temperatures for the different decomposition stages were determined by both the amount of various coke species and the physical structure of the catalysts. The increase in calcination temperature of the catalyst resulted in the increase in combustion temperature of coke, which could be explained from the point of view of the physical properties of the catalyst. The higher the calcination temperature, the stronger the mechanical strength of the catalyst, and the poorer the diffusion of air into and gas out of the core to facilitate combustion, therefore the higher the combustion temperature. As the calcination temperature increased, the decreased weight losses could be attributed to less coke inside the spent catalysts due to the larger and denser particles of the catalysts induced by high calcination temperatures. The increase of the weight of spent 1200-calcin at about 473 °C was due to oxidization of FeCx and Fe3O4 with large particles after combustion of pore-blocking coke, in contrast, spent 500-calcin underwent oxidization of FeCx and Fe₃O₄ at the initial stage owing to its small-sized particles.

The TG-MS results demonstrate that the combustion products of the spent 500-calcin catalyst are CO2 and H2O and show the corresponding trend of the H/C ratio of combusted coke (Fig. 8(D)). Three peaks of CO₂ and H₂O were related to the three decomposition stages of 500-calcin (Fig. 8(A)). The trend of the atomic H/C ratio of each decomposition stage of 500-calcin could be obtained from the peak areas of H₂O and CO2 which demonstrated a decrease from 1.6 to 0.8 to 0.5 (Fig. 8(D)). The highest H/C ratio of the first decomposition stage could be assigned to the combustion losses of adsorbed long chain length wax (soluble coke) on the surface and pores inside the outer layer of the catalyst. The lower H/C ratio of the second decomposition stage could be related to the combustion losses of long chain length wax (soluble coke) and ultra-high molecular mass carbonaceous deposits (insoluble coke) in the blocked pores of the catalyst. The lowest H/ C ratio of the third decomposition stage can be ascribed to

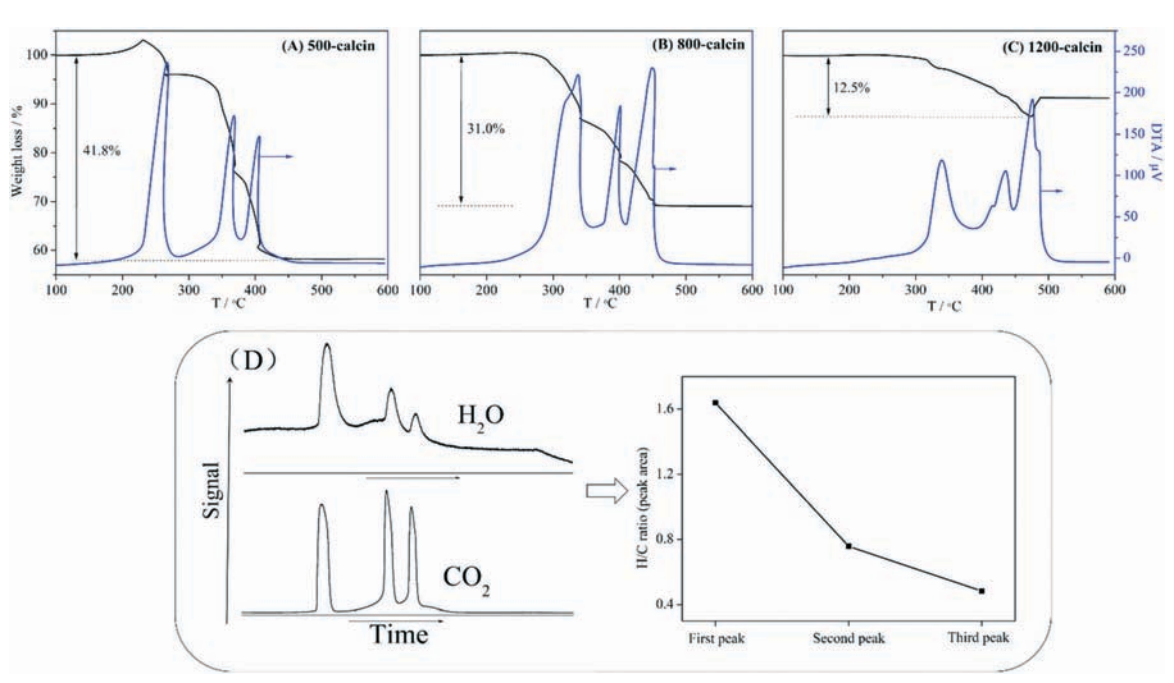


Fig. 8 TG and DTA of spent 500-calcin (A), 800-calcin (B), and 1200-calcin (C) catalysts, and TG-MS of CO₂ and H₂O and the H/C ratio (peak area) (D) of the spent 500-calcin catalyst.

the combustion losses of ultra-high molecular mass carbonaceous deposits and graphitic carbon (insoluble coke) inside the deep channel of the catalyst. The decreasing H/C ratio was also proved by the investigation of Dry who stepwise extracted the spent fused iron catalyst of HTFT with heptane, xylene and pyridine and the atomic H/C ratio of the extracted hydrocarbons decreased from 1.7 to 0.9 to 0.8.9,18 He also confirmed the existence of insoluble coke in the pores of the catalyst by detecting hydrocarbon gases and oils after hydrogen reduction of the pyridine-treated catalyst above 350 °C.

The soluble coke obtained by extraction of spent 500calcin and 1200-calcin catalysts with dichloromethane solvent was investigated. The extracted solution was analyzed by GC-MS, as shown in Fig. 9. The soluble coke of spent 500-calcin and 1200-calcin catalysts demonstrated different hydrocarbon distributions. The soluble coke inside the spent 500-calcin showed a broad distribution of hydrocarbons, and the carbon number could range from 14 to 32, with two maximum amounts at 16 and 22-26 (Fig. 9(A)). However, the carbon number of soluble coke inside the spent 1200-calcin was just between 15 and 21, with a maximum amount at 18 (Fig. 9(B)). The chain growth of hydrocarbons in Fischer-Tropsch synthesis is related to the space of pores inside the catalysts. The mesoporous textural properties of 500-calcin provide more space for chain growth while the more solid physical structure of 1200-calcin contains less space for chain growth.

3.5 Effect of coke formation on catalyst fragmentation

From section 3.4, we can conclude that there are insoluble coke, composed of graphitic carbon and ultra-high molecular

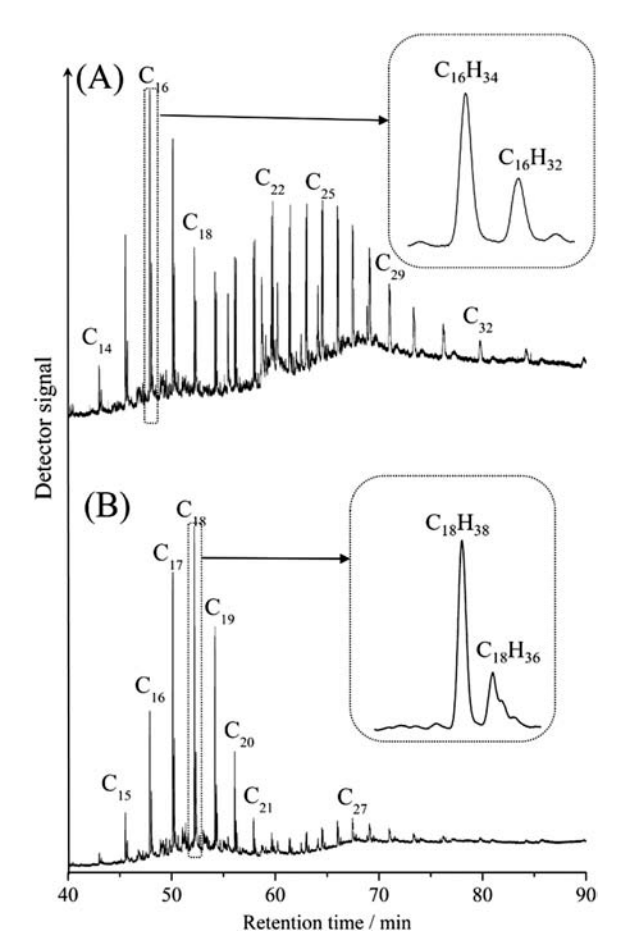


Fig. 9 GC-MS results of soluble coke of spent 500-calcin (A) and 1200-calcin (B) catalysts extracted with dichloromethane solvent.

mass carbonaceous deposits, and soluble coke of long chain length wax inside the spent precipitated iron catalysts. Carbon deposition is extensively considered as the main reason for the fragmentation of iron catalysts. 4,23,28,46,47 Carbon deposition on iron nanoparticles was investigated by Liu through environmental transmission electron microscopy.²⁹ He found trace amounts of graphitic carbon inside iron nanoparticles after 50 min of Fischer-Tropsch reaction at 280 °C, and then, more graphite layers grew out and covered the surface of carbide after continuous reaction for 5 h, causing the carbide crystallites to separate from each other. The rate of carbon deposition increases with increasing reaction temperature, especially above 280 °C. 9,18 In terms of the reaction temperature of 310 °C of the sintered precipitated iron catalysts, the deposition rate of graphitic carbon was fast.

Besides graphitic carbon, the ultra-high molecular mass carbonaceous deposits are also considered as a potential reason for the fragmentation of the catalysts. They can serve as carbon deposition precursors to speed up carbon deposition on the one hand; on the other hand, they accumulate inside the pores of the catalysts which will accelerate the fragmentation of particles. 9,18 Moreover, some long chain length wax may be incapable of diffusing out of the catalyst pores, the continuous build-up of which makes it possible to convert it into even heavier and more viscous carbonaceous deposits. The presence of both carbonaceous deposits and long chain length wax may also lower the reaction rate by slowing down the rate of diffusion of reactants into and products out of the catalyst particles in the long run. $^{9,48-50}$

The schematic process of coke formation of 500-calcin and 1200-calcin is demonstrated in Fig. 10 in accordance with the morphology of the fresh and spent catalysts (Fig. 1 and 7), the coke amount (Fig. 8), and the species of the spent catalysts (Fig. 9). Concerning 500-calcin, the small size of nanoparticles offers more opportunities for carbon deposition, and the mesoporous structure provides more space for accumulation of carbonaceous deposits and the chain growth of wax; simultaneously, the hydrothermal sintering of nano-

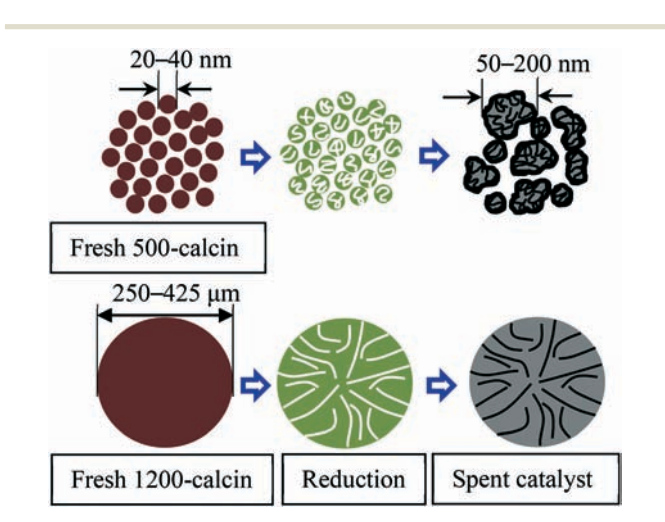


Fig. 10 Schematic processes of coke formation on 500-calcin and 1200-calcin catalysts.

particles may incorporate carbonaceous deposits and wax into the aggregated particles, which further accelerates carbon deposition. In contrast, in the case of 1200-calcin, some pores towards the core are generated on the large-sized sintered particles during hydrogen reduction which provide limited chances for carbon deposition and less space for the accumulation of carbonaceous deposits and the chain growth of wax.

Consequently, the spent traditional precipitated iron catalyst 500-calcin showed a complicated morphology with hydrothermally sintered and fragmented particles. The amount of coke was large and the hydrocarbon distribution of soluble coke was broad. However, the spent sintered precipitated iron catalyst 1200-calcin demonstrated less fragmentation of the catalyst, a smaller amount of coke, and a narrow hydrocarbon distribution of soluble coke. Hence the higher calcination temperature can strengthen the mechanical stability of the catalyst and prohibit catalyst fragmentation, which further improve the occurrence of plugging of the catalyst bed and fouling of the separation equipment.

It is also worth noting that coke deposition can be accelerated by potassium. 9,16,51 In particular, graphitic carbon tends to accumulate at grain boundaries where rich potassium inclusions are found, that is, theoretically, the higher selectivity to lower olefins corresponds to a larger amount of coke deposition and more severe fragmentation of the catalyst. However, the sintered precipitated iron catalysts exhibit both higher selectivity to lower olefins and less fragmentation of catalysts taking advantage of their enhanced fragmentation-resistance ability and less aggregation of potassium during FTO. This strategy might be efficiently used for improving other promoters in iron catalysts or even other solid catalysts.

4. Conclusions

The α -Fe₂O₃ phase of sintered precipitated iron catalysts undergoes transformation to Fe₃O₄ and FeO before being fully reduced to Fe, and their reduction temperatures increase with increasing calcination temperature. For sintered precipitated iron catalysts with calcination temperatures of 800, 1000, and 1200 °C, the maximum activities were achieved at a reduction temperature of 400 °C, while the sintered catalyst calcined at 1400 °C demanded a reduction temperature of 550 °C to maintain high activity. Compared with traditional precipitated iron catalysts, the sintered precipitated iron catalysts demonstrated lower selectivity to methane and higher selectivity to lower olefins due to the suppressed aggregation of potassium by their stronger mechanical strength during reaction. Compared with traditional precipitated iron catalysts which showed a complicated morphology with aggregated and fragmented particles after reaction, sintered precipitated iron catalysts showed a bulk morphology with less fragmentation. The less fragmented morphology of sintered precipitated iron catalysts resulted from their larger-sized particles and higher mechanical strength leading to less

space for the accumulation of coke and chain growth of soluble coke, and further to the smaller amount of coke and shorter chain length of soluble coke. Sintered precipitated iron catalysts exhibit both higher selectivity to lower olefins and enhanced fragmentation-resistance ability, demonstrating potential commercial applications.

Conflicts of interest

There are no conflicts to declare.

Acknowledgements

This work was supported by the second-class General Financial Grant from the China Postdoctoral Science Foundation (2015M571338).

References

- 1 X. Zhou, J. Ji, D. Wang, X. Duan, G. Qian, D. Chen and X. Zhou, Chem. Commun., 2015, 51, 8853-8856.
- 2 W. Di, B. Chen, X. Duan, D. Chen and X. Zhou, J. Energy Chem., 2016, 25, 911-916.
- 3 H. M. Torres Galvis, J. H. Bitter, T. Davidian, M. Ruitenbeek, A. I. Dugulan and K. P. de Jong, J. Am. Chem. Soc., 2012, 134, 16207-16215.
- 4 H. M. Torres Galvis, J. H. Bitter, C. B. Khare, M. Ruitenbeek, A. Iulian Dugulan and K. P. de Jong, Science, 2012, 4, 835-838.
- 5 F. Jiao, J. Li, X. Pan, J. Xiao, H. Li, H. Ma, M. Wei, Y. Pan, Z. Zhou, M. Li, S. Miao, J. Li, Y. Zhu, D. Xiao, T. He, J. Yang, F. Qi, Q. Fu and X. Bao, Science, 2016, 351, 1065-1068.
- 6 K. Cheng, B. Gu, X. Liu, J. Kang, Q. Zhang and Y. Wang, Angew. Chem., Int. Ed., 2016, 55, 4725-4728.
- 7 X. Liu, W. Zhou, Y. Yang, K. Cheng, J. Kang, L. Zhang, G. Zhang, X. Min, Q. Zhang and Y. Wang, Chem. Sci., 2018, 9, 4708-4718.
- 8 L. Zhong, F. Yu, Y. An, Y. Zhao, Y. Sun, Z. Li, T. Lin, Y. Lin, X. Qi, Y. Dai, L. Gu, J. Hu, S. Jin, Q. Shen and H. Wang, Nature, 2016, 538, 84-87.
- 9 M. E. Dry, Chapter 7 FT catalysts, studies in surface science and catalysis, ed. A. P. Steynberg and M. E. Dry, Elsevier Science & Technology, 2004, vol. 152, pp. 533-600.
- 10 A. P. Steynberg, Stud. Surf. Sci. Catal., 2004, 152, 1-63.
- 11 M. Ding, Y. Yang, B. Wu, J. Xu, C. Zhang, H. Xiang and Y. Li, J. Mol. Catal. A: Chem., 2009, 303, 65-71.
- 12 M. Ding, Y. Yang, J. Xu, Z. Tao, H. Wang, H. Wang, H. Xiang and Y. Li, Appl. Catal., A, 2008, 345, 176-184.
- 13 A. P. Steynberg, R. L. Espinoza, B. Jager and A. C. Vosloo, Appl. Catal., A, 1999, 186, 41-54.
- 14 H. Arakawa and A. T. Bell, Ind. Eng. Chem. Process Des. Dev., 1983, 22, 97-103.
- 15 G. C. Maiti, R. Malessa and M. Baerns, Appl. Catal., 1983, 5, 151-170.
- 16 Y. Yang, H. Xiang, Y. Xu, L. Bai and Y. Li, Appl. Catal., A, 2004, 266, 181-194.
- 17 J. Xu, K. Zhu, X. Weng, W. Weng, C. Huang and H. Wan, Catal. Today, 2013, 215, 86-94.

- 18 M. E. Dry and A. P. Steynberg, Chapter 5 Commercial FT process Applications, studies in surface science and catalysis, ed. A. P. Steynberg and M. E. Dry, Elsevier Science & Technology, 2004, vol. 152, pp. 406-481.
- 19 H. Liu, Ammonia synthesis catalysts: practice and theory, Chemical Industry, Beijing, China, 2007.
- 20 G. Ertl, D. Prigge, R. Schloegl and M. Weiss, J. Catal., 1983, 79, 359-377.
- 21 P. M. Loggenberg, M. E. Dry and R. G. Copperthwaite, Surf. Interface Anal., 1990, 16, 347-351.
- 22 E. D. Smit and B. M. Weckhuysen, ChemInform, 2009, 40, 2758-2781.
- 23 E. D. Smit and B. M. Weckhuysen, Chem. Soc. Rev., 2008, 37, 2758-2781.
- 24 W. Ning, N. Koizumi, H. Chang, T. Mochizuki, T. Itoh and M. Yamada, Appl. Catal., A, 2006, 312, 35-44.
- 25 J. Xu and C. H. Bartholomew, J. Phys. Chem. B, 2005, 109, 2392-2403.
- 26 A. Loaiza-Gil, B. Fontal, F. Rueda, J. Mendialdua and R. Casanova, Appl. Catal., A, 1999, 177, 193-203.
- 27 M. A. Vannice, J. Catal., 1975, 37, 462-473.
- 28 M. D. Shroff, D. S. Kalakkad, K. E. Coulter, S. D. Kohler, M. S. Harrington, N. B. Jackson, A. G. Sault and A. K. Datye, J. Catal., 1995, 156, 185-207.
- 29 X. Liu, C. Zhang, Y. Li, J. W. Niemantsverdriet, J. B. Wagner and T. W. Hansen, ACS Catal., 2017, 7, 4867-4875.
- 30 C. Wang, O. Wang, X. Sun and L. Xu, Catal. Lett., 2005, 105, 93-101
- 31 T. Li, H. Wang, Y. Yang, H. Xiang and Y. Li, J. Energy Chem., 2013, 22, 624-632.
- 32 A. Sarkar, D. Seth, A. K. Dozier, J. K. Neathery, H. H. Hamdeh and B. H. Davis, Catal. Lett., 2007, 117, 1-17.
- 33 J. Zhang, K. Fang, K. Zhang, W. Li and Y. Sun, Korean J. Chem. Eng., 2009, 26, 890-894.
- 34 E. Kawasaki, J. Sanscrainte and T. J. Walsh, AIChE J., 1962, 8, 48-52.
- 35 A. Pineau, N. Kanari and I. Gaballah, Thermochim. Acta, 2006, 447, 89-100.
- 36 A. Pineau, N. Kanari and I. Gaballah, Thermochim. Acta, 2007, 456, 75-88.
- 37 M. V. C. Sastri, R. P. Viswanath and B. Viswanathan, Int. J. Hydrogen Energy, 1982, 7, 951-955.
- 38 A. J. H. M. Kock and J. W. Geus, Prog. Surf. Sci., 1985, 20, 165-272.
- 39 J. Zhang, M. Abbas and J. Chen, Catal. Sci. Technol., 2017, 7, 3626-3636.
- 40 G. B. Raupp and W. N. Delgass, J. Catal., 1979, 58, 337-347.
- 41 E. D. Smit, A. M. Beale, S. Nikitenko and B. M. Weckhuysen, J. Catal., 2009, 262, 244-256.
- 42 E. D. Smit, F. Cinquini, A. M. Beale, O. V. Safonova, B. W. Van, P. Sautet and B. M. Weckhuysen, J. Am. Chem. Soc., 2010, 132, 14928-14941.
- 43 A. P. Raje, R. J. O'Brien and B. H. Davis, J. Catal., 1998, 180, 36-43.
- 44 Y. Yang, H. Xiang, L. Tian, H. Wang, C. Zhang, Z. Tao, Y. Xu, B. Zhong and Y. Li, Appl. Catal., A, 2005, 284, 105-122.

Paper

- 45 H. Hayakawa, H. Tanaka and K. Fujimoto, *Appl. Catal., A*, 2006, 310, 24–30.
- 46 A. Dozier, R. A. Khatria, R. Srinivasana, B. H. Davis and U. Graham, Stud. Surf. Sci. Catal., 2006, 163, 101–124.
- 47 A. C. Koeken, H. M. Torres Galvis, T. Davidian, M. Ruitenbeek and K. P. de Jong, *Angew. Chem.*, 2012, 124, 7302–7305.
- 48 R. A. Dictor and A. T. Bell, J. Catal., 1986, 97, 121-136.
- 49 G. B. Raupp and W. N. Delgass, *J. Catal.*, 1979, 58, 361–369.
- 50 G. B. Raupp and W. N. Delgass, *J. Catal.*, 1979, 58, 337–347.
- 51 S. Li, A. Li, S. Krishnamoorthy and E. Iglesia, *Catal. Lett.*, 2001, 77, 197–205.